MTLA 36 (2024) 102163

Contents lists available at ScienceDirect

Materialia

journal homepage: www.elsevier.com/locate/mtla

Microstructural control of LPBF Inconel 718 through post processing of intentionally placed AM discontinuity distributions

E.R. Livera [a,*], K.A. Christofidou [a], J.R. Miller [b], L. Chechik [a,1], D. Ryan [c], J. Shrive [a], I. Todd [a]

[a] University of Sheffield, Department of Materials Science and Engineering, Mappin St, Sheffield City Centre, Sheffield S1 3JD, UK
[b] University of Cambridge, Department of Materials Science and Metallurgy, 27 Charles Babbage Road, Cambridge, CB3 0FS, UK
[c] Solar Turbines Incorporated, 2200 Pacific Highway, P.O. Box 85376, San Diego, CA, 92186-5376, USA

ARTICLE INFO

Keywords:
Nickel superalloys
Laser powder bed fusion
Additive manufacturing
Functional grading
Microstructural control
Bi-modal microstructures
Increased productivity

ABSTRACT

A major untapped potential of laser powder bed fusion (LPBF) is the ability to additively manufacture (AM) parts with site-specific properties. However, robust methods of improving performance and manufacturing efficiency via spatial variations in microstructure are underexplored.

This work investigates a method of creating several distinctive multi-modal microstructures in the nickel superalloy, Inconel 718, by performing a Hot Isostatic Pressing (HIP) procedure on characteristic LPBF discontinuities such as keyhole and lack of fusion (LOF) porosity, as well as large powder filled voids. Observed using electron backscattered diffraction, this approach leads to the formation of site-specific variations in microstructure and extreme bi-modal microstructures. Processing AM parts via this method facilitates the production of fully dense, equiaxed, and strain free material culminating in a substantial time saving per layer. Further optimisation is required in order to achieve an optimum volume fraction and distribution of γ'' precipitates in each heat treated microstructure.

1. Introduction

Metal Additive Manufacturing (AM) enables the production of highly complex metallic parts with fine geometric features, and high strength, directly from a recyclable powder feedstock [1,2]. The process is currently the subject of large volumes of research due to the benefits it promises for manufacturing, such as the ability to produce unique and complex parts. Due to the directional heat dissipation and fast solidification kinetics experienced by the material during processing, the grain structure is typically made up of long columnar grains that span over several layers of the build [2–6]. This produces anisotropic mechanical properties in the build direction [2,6–9]. The extreme processing conditions also commonly lead to the formation of cellular sub-grain structures, stochastic material discontinuities (porosities), and high levels of Type I-III lattice strains. These lead to inferior microstructural stability as well as reduced mechanical properties, especially fatigue resistance and ductility [6,8,10–14]. In addition to this, changes in component geometry lead to further local variations due to changes in the heat dissipation kinetics throughout the part. All of these microstructural effects currently obstruct the qualification of AM parts in advanced engineering applications.

In order to alleviate these issues and increase the efficiency of parts produced by AM, many recent studies have focused on achieving microstructurally tailored parts using AM. Distinctive to the AM process is that the component geometry is manufactured at the same time as the microstructure, both of which can be controlled externally [15]. This enables the production of functionally graded and multi-modal microstructures, facilitating the manufacture of increasingly efficient engineering parts [16–22]. Many innovative methods of locally tailoring the microstructure and its mechanical properties have been proposed across a variety of metallic materials [17-19,21,23–31]. These methods can be loosely categorised by: 1) utilising alternate laser scanning orientations to achieve tailored material textures [23,32], 2) changing the local heat input or energy density to achieve variations in grain size, texture, and phase formation for a variety of different applications including magnetic grading [16,17,19,22,24,26,30,31,33], and 3) utilising post process heat treatments, sometimes in combination with build irregularities, to enable locally varying recrystallisation kinetics for the

* Corresponding author.
E-mail address: elaine.livera@sheffield.ac.uk (E.R. Livera).
[1] New present address for L. Chechik: Institute of Photonic Technologies (LPT), Friedrich-Alexander-Universität Erlangen-Nürnberg, Konrad-Zuse-Straße 3–5, 91,052 Erlangen, Germany.

https://doi.org/10.1016/j.mtla.2024.102163
Received 12 April 2024; Accepted 22 June 2024
Available online 22 June 2024

purpose of, again, controlling the final grain morphology [18,21,23,26,28,29,34,35].

Methods that directly alter the laser parameters such as velocity, power, or alternatively, volumetric energy density, are more at risk to the formation of material discontinuities such as gas, keyhole, or lack of fusion (LOF) porosities [16,22,33]. These cause stress concentrations to form in the material. As the presence and location of these are not visible from the outer surface of the part, they pose an unacceptably high risk to component failure. Additionally, methods which utilise specific laser scanning directions and patterns have been shown to enable variations in build texture to be attained, however the transition between different textures occurs over a considerable distance. For applications where more instantaneous microstructural changes are desired, a different approach may be necessary [32].

Hot Isostatic Pressing (HIP) is regarded as the standard approach for the elimination of material discontinuities in AM [36]. The elevated temperature and pressure applied during HIP enables the collapse and healing of pore walls by plastic deformation and atomic diffusion [37]. The reported ability for HIP to completely eliminate internal pores from the as-built AM material depends on the HIP process parameters chosen, the extent of initial porosity, and the resolution of the analysis in each study [36,38,39]. HIP has also been shown to reduce characteristic AM porosities such as keyhole porosity and lack of fusion (LOF) porosity, as well as densify samples containing large powder filled cavities 2 mm in diameter [38]. One downside is that porosity connected to the surface of the component is not eliminated. This is due to the infiltration of the operating gas and pressure equalisation within the pore [37,38,40–42]. Several researchers have shown that the application of HIP has the potential to promote recrystallisation in as-built AM structures [12,39,43–45], therefore eliminating the columnar grain morphology and homogenising the material. This process has the potential to enable grain structure control as shown by Popovich *et al.* [26]. However, as changes in component geometry and input laser energy density lead to variations in all the types (Types I-III) of lattice strain, proportions of geometrically necessary dislocations (GNDs), elemental segregation, solidification structure, and precipitate distributions in AM parts, the resulting effects of recrystallisation in samples manufactured with 'optimum' process conditions are unpredictable [46].

In addition to the elimination of pores from an AM part, a number of researchers have identified the potential for HIP to generate alternative microstructures in AM samples printed with locally placed voids by recrystallisation. The HIP induced densification of loose powder encapsulated by a dense wall has been shown to produce a fine microstructure in Ti-6Al-4V manufactured by electron beam AM [29], and Inconel 718 manufactured by LPBF [18], with varying degrees of success. Further to this, the HIP consolidation of LOF voids in LPBF Ti-6Al-4V has been shown to enable a bi-modal microstructure consisting of two distinct aspect ratios of α-laths [21]. The authors attribute the observed strength and ductility values, which exceed those of traditionally manufactured counterparts, to this microstructural variability. In Hastelloy-X, the application of HIP on three different volume fractions of LOF porosity has shown that the grain size of the recrystallised microstructure scales inversely with the volume fraction of porosity present [28].

Whilst each of these papers has explored aspects of applying HIP to specific AM discontinuities, no study has systematically investigated the effects of HIP on porosity more broadly, therefore, this paper aims to serve this purpose using the LPBF process and Inconel 718. The source, mechanism of closure, and overall effect on microstructural evolution after HIP of different AM porosities is discussed. This study demonstrates that AM parts can be produced at higher productivity rates, and that these can be easily functionally graded in microstructural terms.

2. Background

2.1. Driving force for recrystallisation

Recrystallisation is the preferred method of reducing lattice strain energy in low stacking fault energy crystal lattices. In AM literature, recrystallisation is commonly attributed to the presence of GNDs due to the long range misorientation they enable [34,47–49]. These may form directly during the build process, or by the post build relaxation of high residual stresses associated with the process. In addition to the GNDs, it is likely that the volume of all types of lattice strain (Types I-III) [50] contribute to the recrystallisation process.

Materials such as 316 L stainless steel [47,51–54] and Inconel 738LC [34], manufactured by AM, contain dislocation densities in the order of 10^{14} m^{-2}. Of these, the number of GNDs present in a material can be estimated using kernel average misorientation (KAM) maps obtained from EBSD data [34,47]. Peachey *et al.* [34] rationalise that the majority of dislocations stored in as-built AM parts are GNDs, instead of statistically stored dislocations. This is because in AM parts, the directional and epitaxial nature of grain growth leads to the formation of large grains inclusive of solidification cells with intercellular elemental segregation [10]. Subsequent heating and cooling (expansion and contraction) of this non-equilibrium microstructure leads to the formation of high GND density at these inter-cellular regions [53]. For a given material, the density of these has been shown to increase with an increased level of material constraint during the build process (e.g. larger parts, higher complexity parts, deeper melt pools) [55], through the use of processing parameters that produce a finer cellular solidification structure [34], or through external plastic deformation [46,56].

The total volume of strain present influences not only the minimum temperature required for the onset of recrystallisation but also the speed at which it takes place [49,55,57]. At lower total bulk stain values, fewer nuclei will be formed, and more time is required for a nucleus to form. As there is a lower density of rapidly growing nuclei, the resulting grain morphology is therefore larger than for a lattice inclusive of high strain [56].

Therefore, due to the multitude of controllable factors in the AM process, the total lattice strain in different AM parts will not be equal [47], leading to contradicting information on the post build heat treatment type, duration, temperature, and additional deformation, required to attain recrystallised material in Inconel 718 [12,39,43–45,47,58–61]. Generally, further deformation, either through HIP [12,39,43–45] or other mechanical means [23] produces a greater probability of attaining a fully recrystallised microstructure due to the increase in lattice strain produced.

As well as lattice strain, another form of 'energy' present in AM parts is that associated with free surfaces in the vicinity of grain boundaries or internal voids [37,62]. The energy associated with grain boundaries provides the driving force for grain growth after recrystallisation at elevated temperatures. The energy associated with free surfaces at internal voids is understood to be the driving force behind pore healing during the HIP process [37,63].

2.2. Nucleation of recrystallisation nuclei

Recrystallisation nuclei can be produced by one of a number of different processes; grain boundary bulging [57,64–69], sub-grain growth [66,70], as a result of twin formation during annealing (grain growth), or deformation [23]. Whilst twin boundary formation during annealing is a method of forming a recrystallisation nucleus on its own accord [46,65], the formation of twins has also been rationalised to facilitate recrystallisation by acting as obstacles to further dislocation motion, leading to large strain gradients [47,71]. Under the application of continuous load as well as elevated temperature, as is the case for the HIP process, the recrystallisation process may repeat continuously [64].

The formation of low coincident site lattice (CSL) boundaries during

the recrystallisation process is important to specific mechanical properties such as creep and corrosion [46]. As these are typically produced by growth accidents, a finer initial grain size enables more twin boundaries to be produced for a given volume of stored energy [72]. Similarly, a higher level of deformation for an equal grain size produces a higher driving force for the HAGB migration, producing more twin boundaries.

3. Experimental details

An AconityMINI (Aconity3D, Germany) was used to print four sets of cylindrical samples using 15–45 μm diameter gas atomised Inconel 718 powder (LPW, batch number UK83045). Each cylinder measured 8 mm in diameter, by 10 mm high. A fully dense outer shell contained a 6 mm diameter, 6 mm tall, internal cylinder in which the printing parameters were altered to produce either, fully dense material, keyhole discontinuities, LOF discontinuities, or 3 internal spherical cavities, 2 mm in diameter, holding unmelted powder. Three identical cylinders were produced in each set. The process was performed under an Argon atmosphere and printing parameters, along with a value for the volumetric energy density [73], are detailed in Table 1. For all samples, a simple back and forth raster laser scanning strategy was utilised. The samples are designated as follows: Dense, Keyhole, LOF and Sphere. When the AM consolidated section of the Sphere sample is discussed, this is referred to as Sphere Bulk, whereas the loose powder consolidated during HIP is referred to as the Sphere Void.

Four samples in each set underwent HIP (1160ºC / 102 MPa / 3 h / air cool) with a temperature ramp up rate of 10 °C/min, and of these, two samples in each set underwent post HIP solution heat treatment (980 ºC / 1 h / air cool), and a double age heat treatment (720ºC / 8 h / furnace cool / 620ºC / 8 h / air cool) under an argon atmosphere. Samples are referred to as as-built if they did not undergo any heat treatments, and HIP, or HIP + HT if they underwent only HIP or both HIP and full heat treatment respectively.

Samples were cross sectioned parallel to the build direction in the as-built, HIP only, and HIP + HT states by wire electrical discharge machining (EDM), and polished to a mirror finish using standard metallographic preparation techniques, culminating in a polishing step utilising colloidal silica suspension with a particle size of 0.04 μm.

Observation of the internal discontinuity structures across the whole as-built sample discontinuity region was performed using an optical microscope fitted with a Clemex Vision camera and imageanalysis software. Information on the discontinuity shape characteristics was acquired using an automatic thresholding technique in Fiji ImageJ [74]. Mean feret lengths were calculated by fitting a log-normal distribution to the dataset.

Electron backscattered diffraction (EBSD) was performed in a JEOL 7900F SEM with an accelerating voltage of 20 kV, a probe current (spot size) of 14, a focus depth of 21, and a step size of 1 μm (HIP + HT Sphere sample used step size of 1.5 μm), to analyse the grain orientations within each sample. Concurrently, Energy Dispersive X-Ray Spectroscopy (EDX) analysis was performed in order to identify precipitates in each microstructure. At least 2000 grains were captured for EBSD grain analysis in each sample (HIP Sphere Bulk region used 500 grains for analysis). Image reconstruction and analysis was performed on MATLAB using the MTEX toolbox [75]. Threshold orientations of 10°, and 3° were used to define the high angle, and low angle grain boundaries respectively [62]. Following the removal of grains smaller than 3 pixels, the grains were reconstructed and all non-indexed locations removed. Maps showing grain orientations, Kernal Average Misorientation (KAM), and Σ3 boundaries were produced from the reconstructed EBSD data. Grain area and grain diameter data were determined for each sample through standard functions in MTEX. The metric of grain 'area' was primarily utilised to evaluate the grain size throughout the study as this provides a representative comparison between the samples as the grains change in shape due to recrystallisation. The area percentage taken up by each grain size range is plotted for each sample using a bin size of 500 μm. For the consolidated powder regions, a bin size of 50 μm was implemented. In order to aid the visualisation of the differences in grain size between each sample, values for the mean grain diameter were evaluated using MATLAB by fitting a lognormal distribution function to the MTEX grain diameter dataset. The standard method of calculating grain diameter in MTEX is by calculating the longest distance between two edges of a grain. This was considered an effective method of evaluating grain size as a large proportion of the grains are not perfectly round. Finally, the percentage of Σ3 boundaries was calculated for each sample to determine what percentage of the total grain boundary length was taken up by Σ3 boundaries.

Samples were electrolytically etched using a 10 % by volume phosphoric acid to water solution, and a voltage of 5 V, in order to reveal the precipitate morphology for each build condition in the as-built, HIP and HIP + HT states. SEM analysis was performed using an Inspect F50 with an accelerating voltage of 20 kV and a spot size of between 3 and 3.5 μm.

Transmission electron microscopy (TEM) samples were produced from the HIP + HT samples by focussed ion beam (FIB) machining using a gallium ion source. Samples were extracted from grains orientated with their [100] direction perpendicular to the sample surface in order to make the identification of precipitates from the electron diffraction patterns easier. TEM of the FIB samples was performed using a FEI Tecnai Osiris, operated at 200 kV. STEM bright field images were acquired of the FIB specimens, with selected area electron diffraction patterns collected using a Gatan 4 K camera.

Vickers hardness information was gathered on the same samples using a Durascan 70 automatic hardness testing machine using a 15 s dwell time and HV1 load which corresponds to a load of 1 kg/f.

Table 1
Laser process parameters used to manufacture the discontinuity cylinders.

	Laser Power (W)	Laser Velocity (mms^{-1})	Hatch Spacing (μm)	Layer Thickness (μm)	Volumetric Energy Density (J/mm^3) [100]
Dense	130	850	75	30	68
Keyhole	166	582	42	30	226
LOF	94	1118	108	30	26

4. Results

4.1. Morphology of as-built discontinuity structures

A laser power of 130 W, velocity of 850 mm/s, and hatch spacing of 75 μm, enables nominally fully dense material to be produced with a density of 99.98 % (Fig. 1). Quantitative porosity analysis, displayed in Figure A of the Supplementary Data, shows that a small number of fine circular (mean 6.8 μm, variance 18.4μm^2) gas pores are still present in the central region of the Dense cylinder. These pores are known to originate from the metal powder, or can become incorporated into the material by entrapment of the process gas during printing [76].

An intentional increase in power, and decrease in velocity and hatch spacing to 166 W, 582 mm/s, and 42 μm respectively, leads to the formation of keyhole porosity (99.66 % density) with a mean Feret length of 23.1 μm (variance 399 μm^2) and a circularity of 0.9 ± 0.1. Figure A of the Supplementary Data shows that the Keyhole porosity is less homogeneous in size compared to the gas pores visible in the dense sample. Fig. 1 shows that the pore size increases nearer the shell region due to the increased heat generated during the laser turn function in the meander scan strategy. This effect is understood to have enabled a slower cooling rate at cylinder edges compared to the centre of the internal cylinder.

A power, velocity, and hatch spacing of 94 W, 1118 mm/s, 108 μm respectively, leads to a homogeneous distribution of lack of fusion (LOF) porosity, with a global density of 91.49 %. Pore sizes are much larger

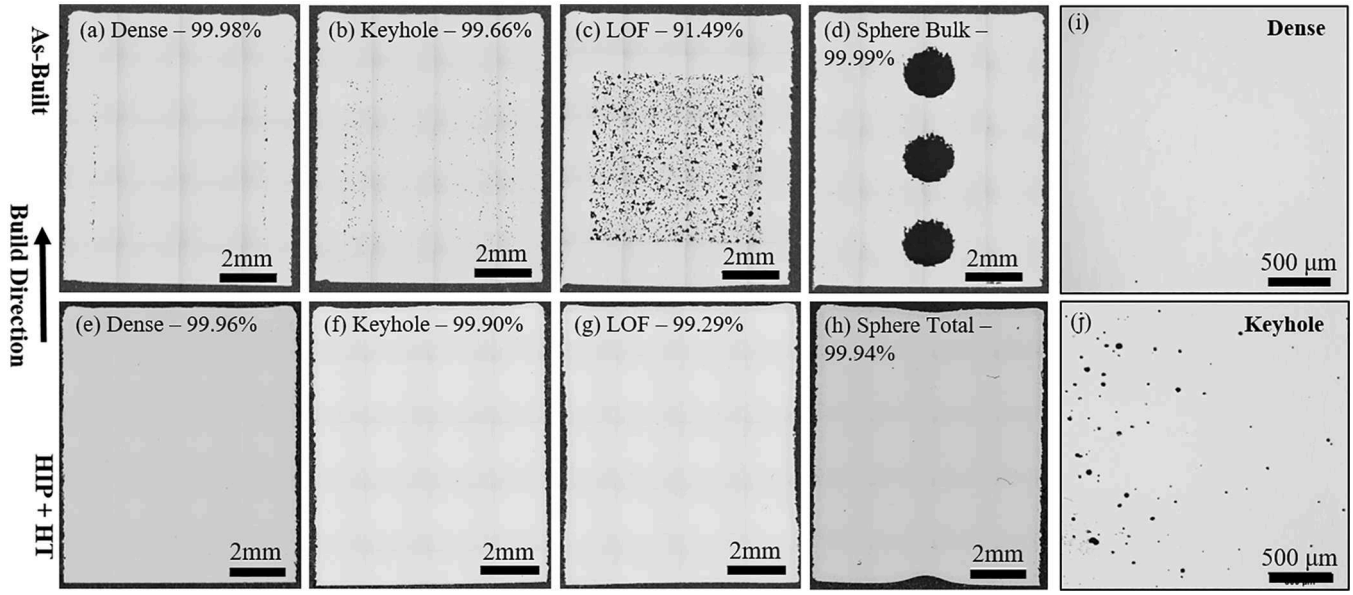

Fig. 1. Optical micrographs of the cross section of each cylindrical sample. (a) – (d) shows the as-built samples containing the associated internal discontinuity structures and (e) - (h) shows the samples after HIP + HT. All samples observed full densification by the heat treatments performed. (i) shows a closer image of the void region of the Dense sample and (j) shows a closer image of the Keyhole sample. A clear difference in internal discontinuities can be observed despite the small difference in calculated density.

than those in both the Keyhole and Dense samples, and are much less circular in shape. A small number of very large pores in Figure A of the Supplementary Data indicates a high level of pore connectivity.

A line of discontinuities can be observed between the cylinder shell and internal region in the Dense sample. These are due to insufficient overlap between the two surfaces. As they are assumed to be present in each sample, all grain structure analysis post heat treatment was performed in the central region of the internal area so as to not include these discontinuities in concluding analysis.

Densities of the Dense, Keyhole, LOF and Sphere samples after HIP + HT were 99.96 %, 99.90 %, 99.29 % and 99.94 % respectively. Depressions are observed in the top and bottom of the Sphere sample as a result of plastic deformation by the isostatic pressure on the hollow spherical regions.

4.2. Grain structure of the as-built, HIP and HIP + HT samples

4.2.1. As-Built state

Inverse pole figure (IPF) maps with respect to the building direction are shown in Fig. 2 alongside electron microscope images of each sample in the as-built state. All samples exhibited elongated grains as a result of epitaxial growth from the melt pool, with many grains observing internal misorientations facilitated by the presence of GNDs. A clear difference in the grain areas between each sample in the as-built state is also exhibited. Quantitative analysis of the grain area for each sample in the as-built, HIP and HIP + HT states is shown in Figure B of the Supplementary Data.

In the LOF sample, the extensive network of discontinuities resulted in local disturbances to the epitaxial grain growth process, which consequently led to the presence of a high volume of small, more randomly orientated grains surrounding the irregular void regions [22]. Similarly, clusters of finer grain sizes are also observed at locations near keyhole pores, however, to a lesser extent. Partially melted powder particles, which have retained their fine grain morphology, reside within the LOF void regions.

All samples exhibited cellular sub-structures typical of the AM process in the as-built condition, with these being visually coarser in the Dense and Keyhole samples compared to the LOF sample. In addition to this, there is a wider intercellular segregated region in the Keyhole sample compared to the other samples. Solidification structures immediately surrounding both Keyhole and LOF discontinuities are shown in Fig. 2e)-g), showing the difference in scale of the solidification structures near each discontinuity. KAM maps for the void regions in the LOF and Keyhole samples in the as-built state are shown in Fig. 2 (h-i). It is clear that elevated levels of dislocation accumulation are present at regions immediately surrounding the voids in both samples. Kasperovich et al. [77] have shown using x-ray computed tomography that both Keyhole and LOF voids have ripples in their internal shape morphology. These ripples observe high levels of curvature which may have a higher propensity for stress concentrations to form during successive heating cycles as the next layer is printed, leading to an increase in local dislocation density.

Fig. 3 shows the presence of a significant level of intra-grain misorientation (enabled by high dislocation activity) within each sample in the as-built state, as well as the presence of limited $\sum 3$ boundaries.

4.2.2. HIP and HIP + HT processed states

IPF maps with respect to the building direction for each sample after HIP and HIP+HT are shown in Figs. 4 and 5 respectively. Electron microscopy images for each sample showing the precipitate structures for each condition are also presented in the figures. As expected, the major changes in the grain shape morphology took place during HIP with minimal changes occurring during further heat treatment. This secondary heat treatment instead allowed evolution in the precipitate structures. Fig. 6 shows EDS maps of each sample in the HIP + HT states in order to identify precipitates in the microstructure.

After HIP and further heat treatment, the Dense sample largely retained the as-built elongated grain morphology and large extent of sub-grain misorientations. The grain area (Figure B of the Supplementary Data) remained similar to the as-built state throughout the work. Fine patches of recrystallised material (~50–100 µm), as presented by a local decrease in KAM intensity in Fig. 3(a), indicate the presence of stochastic recrystallisation within the dense sample. Negligible amounts of $\sum 3$ boundaries were present in the Dense sample after HIP or HIP + HT.

Comparison of the SEM images of the Dense sample before and after HIP (Figs. 2 and 4), shows a breakdown of the interdendritic segregated

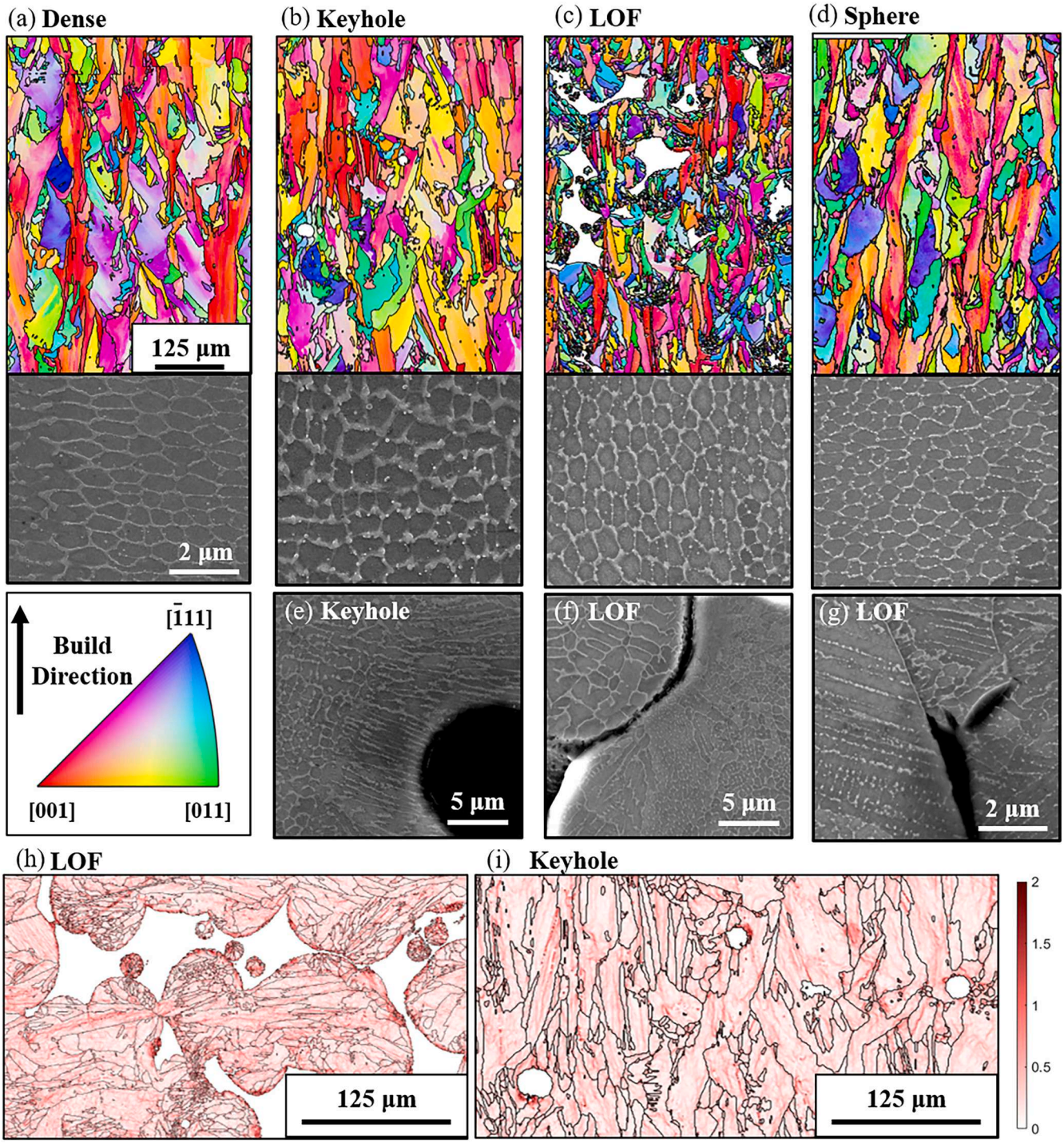

Fig. 2. EBSD IPF maps with respect to the building direction for the as-built Dense, Keyhole, LOF and Sphere samples shown alongside electron microscopy images of the sub-grain structures. All samples show elongated grains that have grown in the preferential [001] crystal growth direction which is aligned with the build direction. The LOF sample observes a finer grain structure, both in width and length of the grains, as compared to the Dense, Keyhole, and Sphere Bulk samples, with unmelted powder particles present in the vicinity of the LOF voids. Regions surrounding voids in the LOF sample have a more random selection of grain orientations. All samples show a cellular sub-grain structure, with the interdendritic material being coarser in the Keyhole sample as compared to all other samples. Images (e)-(g) show the microstructural features surrounding the intentionally placed discontinuities. Images (h) and (i) show KAM maps of the void regions in the LOF and Keyhole samples. Misorientation on the colourbar is in °. Elevated regions of KAM are observed surrounding internal voids indicating a high dislocation density gradient in these regions.

sub-structures after HIP, with an emergence of likely MC carbides and δ phase precipitates at prior cell boundaries [78]. Further HT promoted the growth of the δ phase at grain boundaries, with γ″ particles precipitating within the grains. Higher resolution SEM and TEM images comparing the γ″ precipitates present in each sample after HIP + HT are shown in Fig. 7 and will be discussed later.

Whilst the majority of the Keyhole sample maintained a columnar grain morphology with similar grain area (Figs. 4 and 5) after HIP and further heat treatment, large discontinuously recrystallised grains (250–300 µm in diameter) are located in the vicinity of previous keyhole

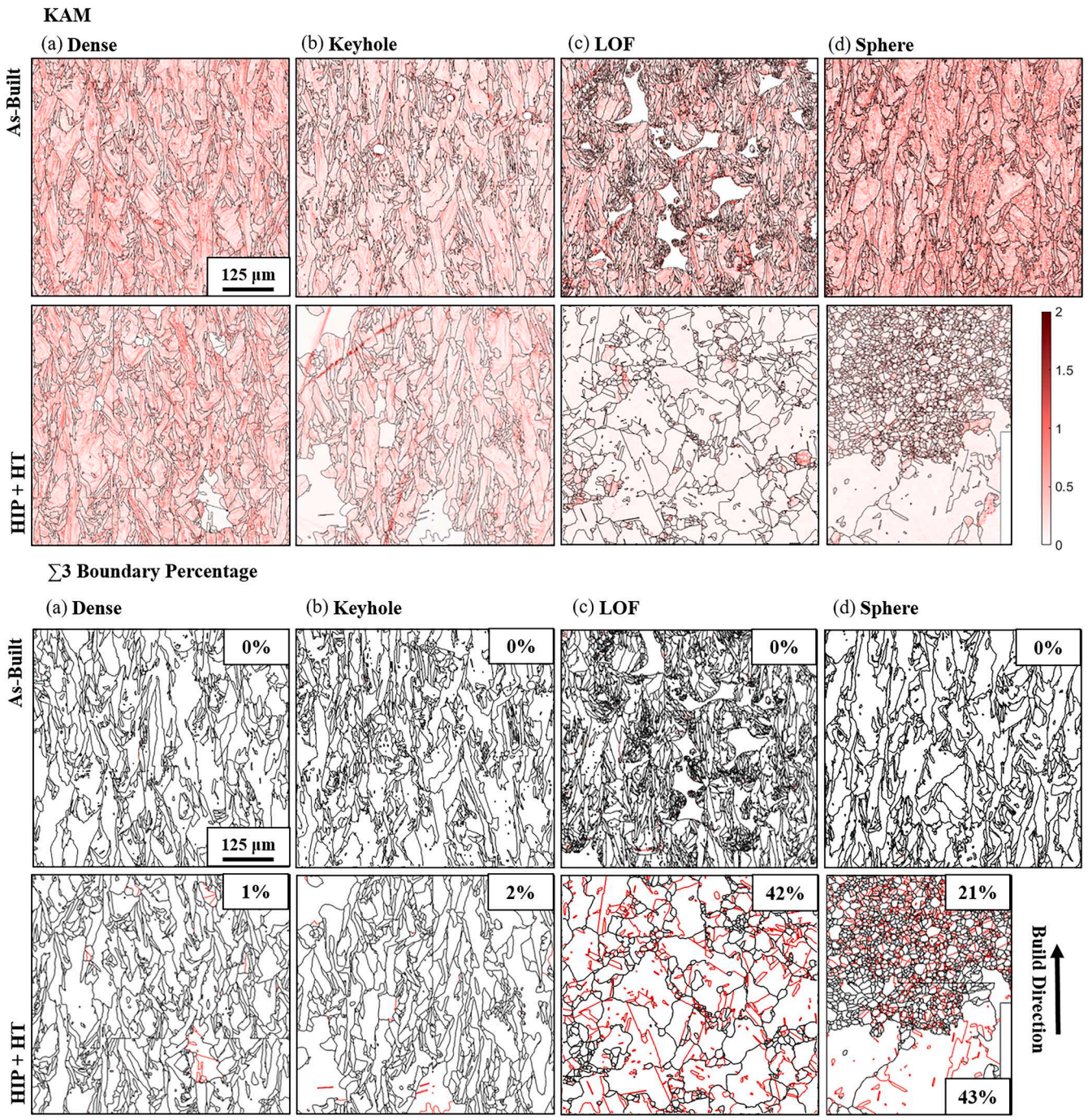

Fig. 3. Comparison of the KAM maps (misorientation on the colourbar is in °) and twin boundary maps of each sample in the as-built and HIP + HT. All ∑3 twin boundaries are highlighted in red, with all other boundaries coloured in black. After HIP + HT, the LOF and Sphere samples show a distinct reduction in the volume and size of sub-grain misorientations, and increase in twin boundary fraction, due to recrystallisation. The sub-grain misorientations in the Dense and Keyhole samples remain similar to before HIP and HT, with the exception of pockets of recrystallised material located stochastically throughout the Dense sample, and the presence of large recrystallised grains on the edge of the imaged area in the Keyhole sample.

voids. These large grains have an associated decrease in KAM (Fig. 3) as compared to the rest of the HIP and HIP + HT sample and contain twin boundaries. Minimal twin boundary formation is observed outside these recrystallised grains. The recrystallised microstructure is free from solidification cells after HIP, with γ″, MC carbide, and δ phase particles having emerged after further heat treatment.

The LOF and Sphere samples both underwent near complete recrystallisation during HIP resulting in a more equiaxed grain morphology with a decrease in KAM and a large increase in the ∑3 boundary fraction (from 0 % to >42 %). The prior grain orientation preference in the build direction was also reduced. The grain area of the LOF and Sphere Bulk samples greatly increased after HIP.

In the LOF sample, the majority of the discontinuities have been consolidated, with only a very small fraction of pores still present in the material. Evidence of a previously unmelted powder particle is present in the surrounding recrystallised material after HIP (Fig. 6), and several inter- and intra-granularly placed carbides can be observed [79]. As oserved from the EDS maps of the HIP + HT samples in Fig. 6, these are likely MC type carbides. Evidence of large scale discontinuous precipitation of the δ phase can be observed at grain boundaries, alongside the

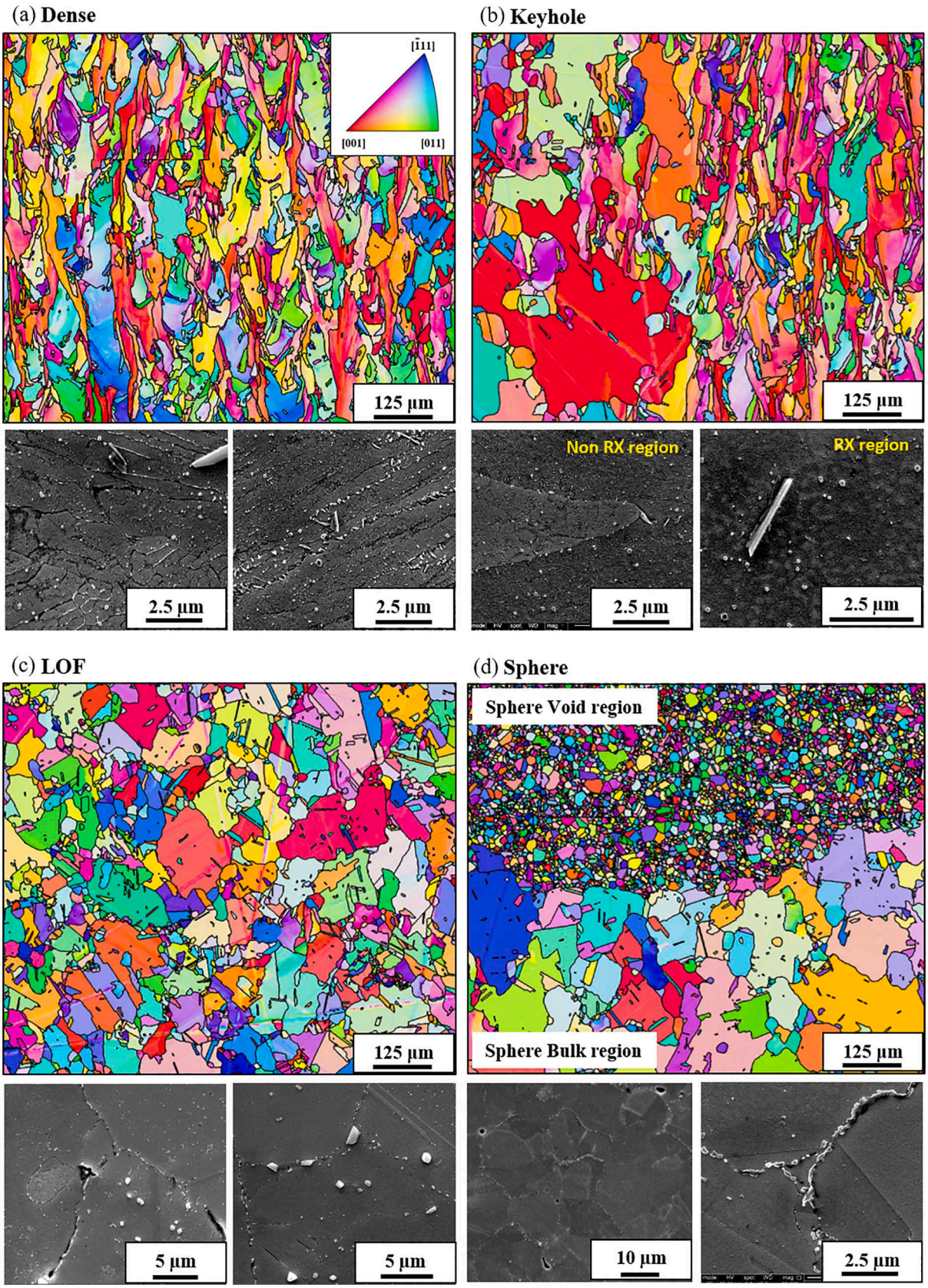

Fig. 4. EBSD IPF maps with respect to the building direction for the Dense, Keyhole, LOF and Sphere samples subject to HIP only. Note the difference in scale on the Sphere map. The Dense and Keyhole samples still show the elongated nature of as-built AM grain structures with a general orientation in the [001] direction. Large recrystallised grains are visible in the Keyhole sample. The LOF and Sphere samples show a more equiaxed microstructure, have a more random mix of grain orientations, and observe a bi-modal microstructure to two different extents.

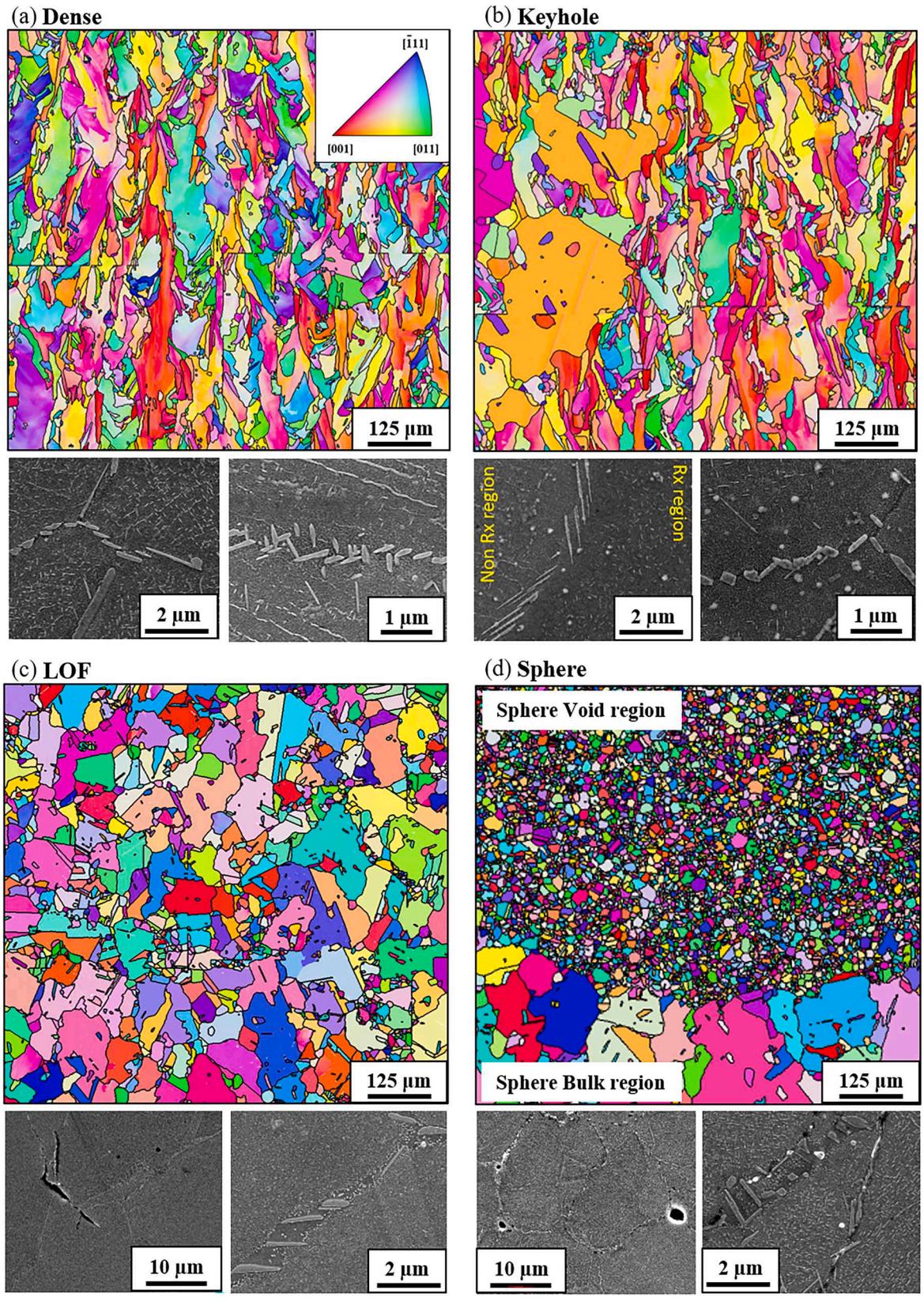

Fig. 5. EBSD IPF maps with respect to the building direction for the Dense, Keyhole, LOF and Sphere samples subject to HIP and heat treatment. Note the difference in scale on the Sphere map. The Dense and Keyhole samples still show the elongated nature of as-built AM grain structures with a general orientation in the [001] direction. Large recrystallised grains are visible in the Keyhole sample. The LOF and Sphere Void regions are visibly unchanged from the HIP state. The grains in the Sphere Bulk region are visibly larger after HIP + HT than HIP only.

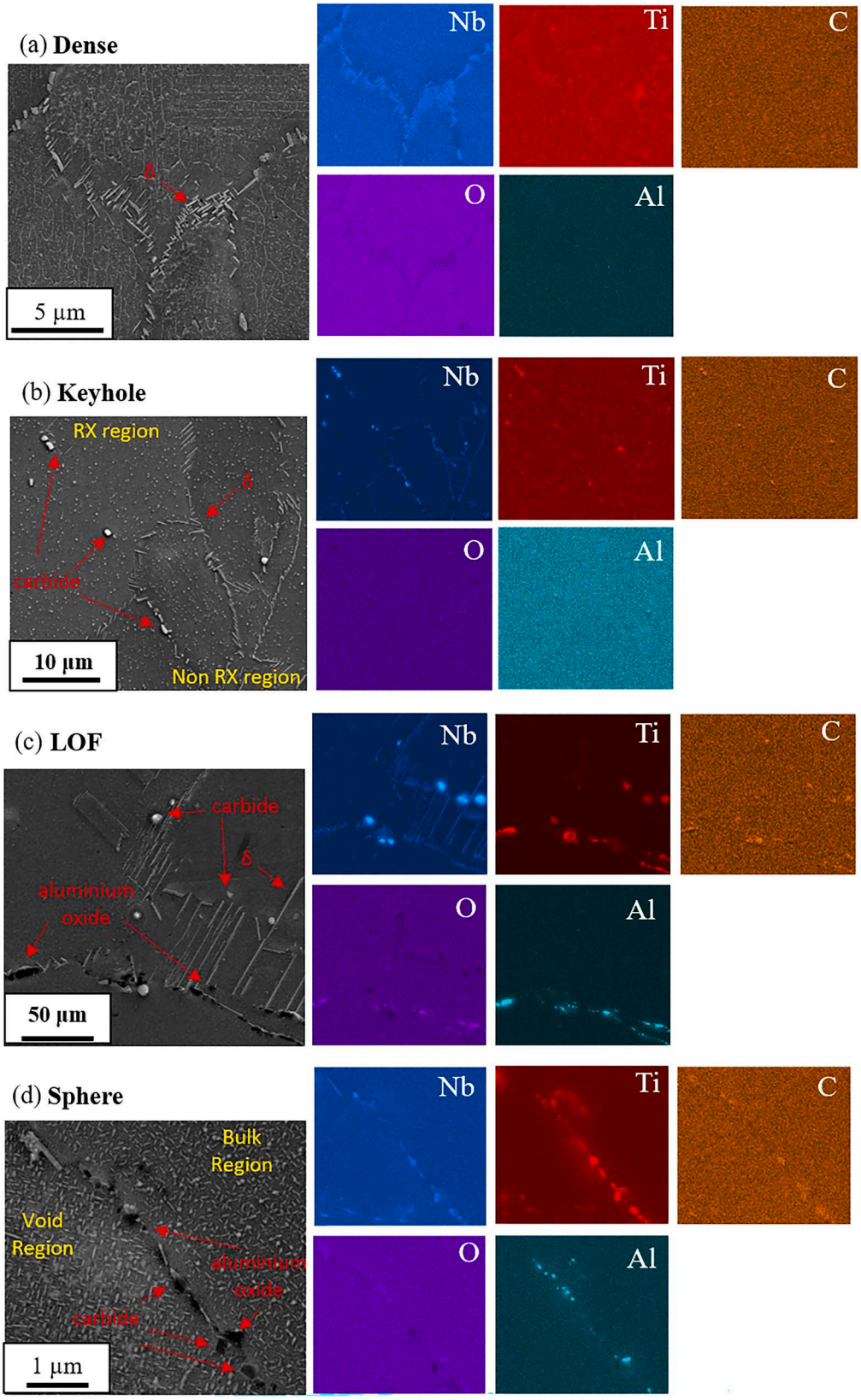

Fig. 6. SEM EDS maps for each sample in the HIP + HT states showing the presence of δ phase, and Nb or Ti based MC carbides, at grain boundaries. In both the LOF and Sphere samples, the inclusion of Al oxide is shown. For the Sphere sample this was observed between powder particles in the Sphere Void region as well as at the interface between the Sphere Void and Sphere Bulk regions. In the LOF sample, Al oxides are believed to be present at the prior LOF void interfaces. The inclusion of Al oxides in these regions are believed to be due to the presence of unmelted powder particles in the as-built material.

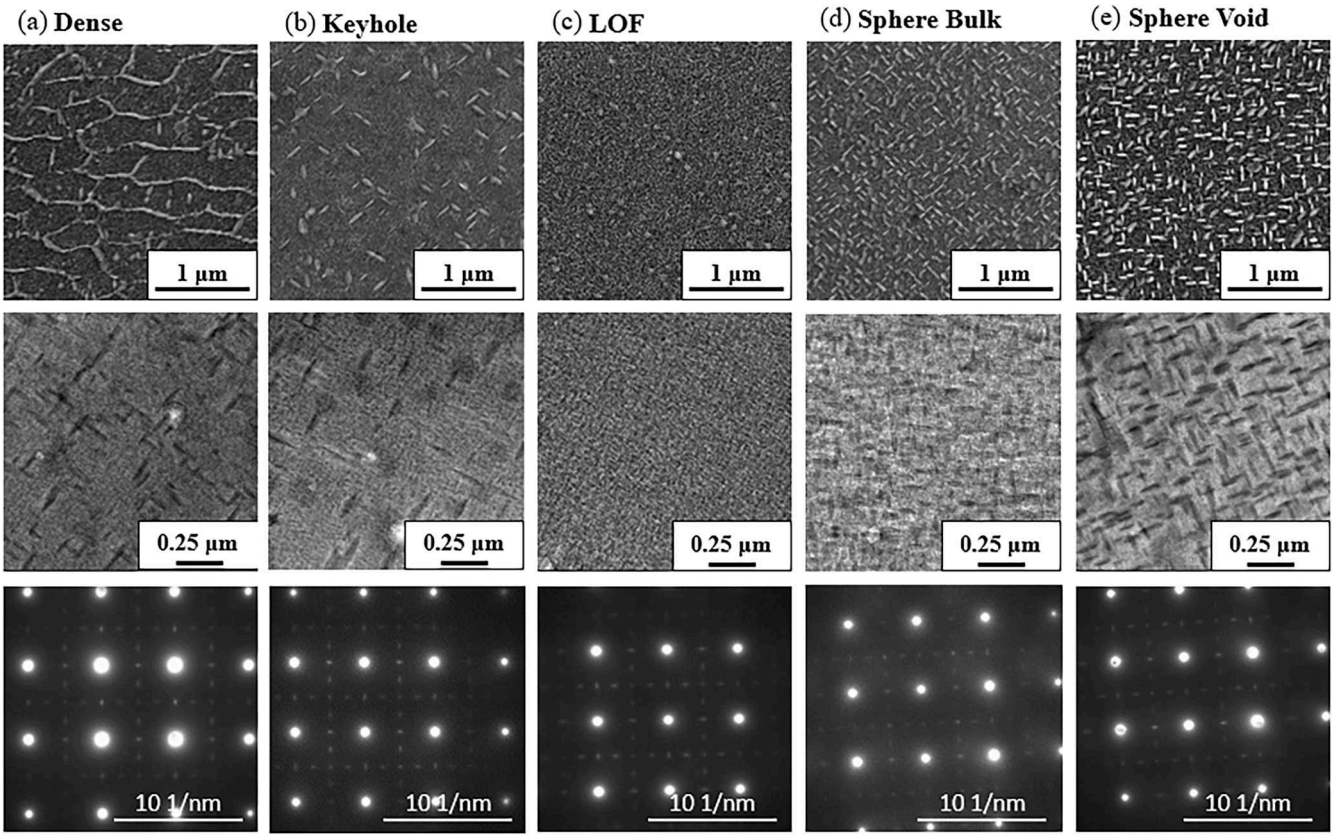

Fig. 7. Intergranular precipitate structures for each sample showing the distribution of γ″ precipitates. Top row, SEM data, middle row, STEM bright field micrographs, bottom row, selected area electron diffraction (SAED) patterns for all samples from the ⟨100⟩ matrix zone axis showing the clear presence of γ″ precipitates.

presence of carbides and, in some cases, Al or Ti oxide particles. Only very fine γ″ precipitates are present within the grains. These can only be detected by TEM EDS analysis as presented in the next section.

In the sphere sample, a large difference in grain size is observed between the Sphere Bulk and Void regions. In the final HIP + HT condition, the grain diameter of the Sphere Bulk region is 187 % larger than the Void region. The prior void regions of the Sphere sample in the HIP + HT condition contain prior particle boundaries (PPB), decorated by fine carbides, δ phase, and aluminium oxide particles (Fig. 6). The δ phase particles are not observed in the HIP only condition. Fine pores (~1–2 µm) can be observed at prior particle triple points in both heat treated conditions. Intergranular regions contain a homogeneous distribution of γ″ precipitates in the HIP + HT state.

The observed Al oxide particles present in the LOF and Sphere samples are likely due to the presence of unmelted powder particles in these samples [18].

After HIP + HT, the grain diameters of the Dense, Keyhole, LOF, Sphere Bulk and Sphere Void samples were calculated to be 25.9 µm, 27.0 µm, 18.2 µm, 29.3 µm, and 10.2 µm respectively. The variance of each of these values were approximately 1100 μm^2, 1200 μm^2, 440 μm^2, 2200 μm^2 and 50 μm^2, respectively. This shows that the grain diameters in the LOF and Sphere Void samples are overall finer, and more homogeneously distributed, than in the Dense and Keyhole samples.

4.2.3. γ″ phase structures after HIP + HT

Intergranular precipitate structures for each sample are shown in Fig. 7 along with selected area electron diffraction (SAED) images from the ⟨100⟩ zone axis showing the clear presence of γ″ precipitates [80,81]. All recrystallised regions of material contain a uniform distribution of γ″ precipitates, however the volume fraction and size of these differs between each sample. The Dense and Keyhole samples contain more dispersed, and larger, γ″ precipitates compared to the LOF and Sphere samples that underwent complete recrystallisation. In addition, the larger scale image of the Dense sample still clearly shows the presence of segregated material at the cell boundaries. This is due to the lack of recrystallisation and homogenisation of the segregated elements in this sample. All other images displayed in Fig. 7 were taken from recrystallised regions of each respective sample. The impact of these differences on the hardness of the samples is discussed in Section 4.3.

It is clear from these results that following the HIP processing of materials built to include different discontinuity structures, a tailored post process heat treatment is required in order to precipitate an optimised volume fraction of strengthening precipitates.

4.3. Sample hardness

Hardness measurements for each sample are shown in Fig. 8. In order to prevent damage to the indentor tip from accidental porosity indentation, the hardness of the as-built LOF sample was not measured. The Dense and Keyhole samples exhibited a slight drop in hardness after the HIP process, although this value is within the calculated experimental error. The Sphere Bulk sample decreases in hardness by about 100 Hv after HIP, with the LOF sample observing the same hardness. After HIP + HT, the hardness of all samples increased to between 441 and 461 Hv. Consideration has to be made to the fact that only ~¼ of the number of hardness measurements could be taken for the Sphere Void region as opposed to other samples due to the small area encompassed by the region.

5. Discussion

Due to the fast solidification conditions in AM, all samples observed directional solidification encompassing long columnar grains, with cellular sub-grains, in the as-built state. Each sample is understood to

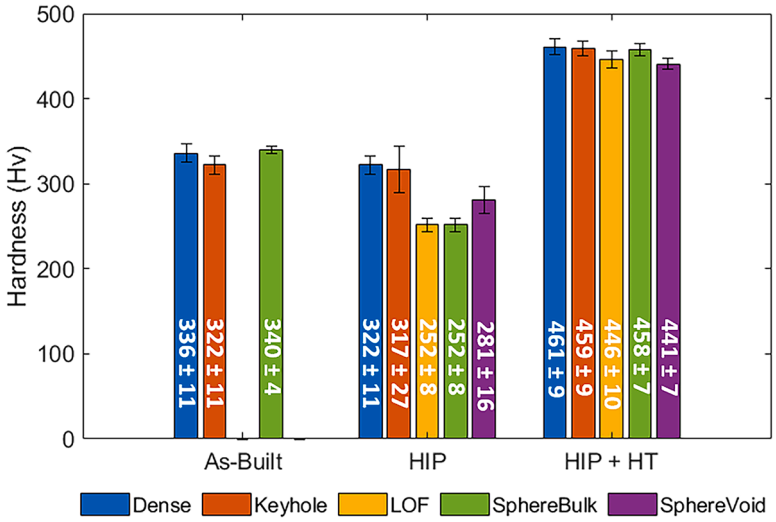

Fig. 8. Hardness measurements for each sample in the as-built, HIP and HIP+HT states.

comprise of a different level of inherent lattice strain. This is due to a number of factors including the differences in the LPBF process parameters used to build them, the introduction of different characteristic AM voids, and differences in the sample laser scanning geometry (Sphere sample). The rainbow effect in the IPF maps in Fig. 2 as well as the misorientation data displayed in the KAM maps in Fig. 3 both distinctly exhibit the presence of GNDs present within each grain. The introduction of characteristic AM porosity also acted to hinder epitaxial growth leading to a local refinement of the microstructure (increasing the local grain boundary energy [62]). This is especially evident in the LOF sample. Sharp internal features within these void regions [77], likely led to stress concentrations during subsequent heating and cooling cycles, enabling the accumulation of GNDs, further locally enhancing the local lattice strain in the Keyhole and LOF parts.

All samples underwent a HIP procedure in which plastic deformation and diffusion occurred [82]. Differences in the internal densities and spatial location of each porosity type within each sample in the as-built state led to differences in the volume, spatial location, and speed of plastic deformation. Therefore, the corresponding strain accumulation for each sample also differed in magnitude and spatial location [83,84]. As a result, each sample attained a very different grain morphology and distribution after the HIP process, demonstrating the potential for different intentionally placed discontinuities to be used to produce functionally graded components.

The fine, equiaxed, and bi-modal, recrystallised grain morphology in the LOF sample is a result of a combination of, high (and bi-modal) grain boundary density, high complexity internal pore shapes (leading to local stress concentrations and increased dislocation activity), and high levels of plastic deformation during HIP [21]. All of these factors led to a high driving force for recrystallisation in this sample. The high laser velocity used to build this sample may also have led to an increase in GNDs present in the as-built state compared to the other samples This is due to the relative reduction in recovery possible at the increased cooling rates, as well as the increase in material constraint provided by the dense cellular segregation structure [34,47,51]. Gao et al. [47] showed that an increase in laser velocity led to the formation of a finer cellular structure and an increased level of solute trapping at the cell boundaries, leading to the reduction in twin boundary formation during plastic deformation, and a resulting decrease in the nucleation of recrystallised grains. However, the large volume of plastic deformation that occurred in this sample in order to fuse the void regions, still enabled a high level of recrystallised grains to be produced. Combined with the overall finer initial grain size, the LOF sample was able to attain an overall finer grain morphology compared to that observed in the Keyhole or Sphere Bulk samples.

The bi-modal recrystallised grain morphology achieved in the LOF sample is similar to the formation of recrystallisation necklace structures along deformation planes observed in Inconel 718 [85,86]. Nano-sized bi-modal microstructures have been shown to exhibit a combination of both high strength and ductility, potentially making this a valuable method of AM microstructure manipulation [87]. Similarly, further optimisation of the HIP and heat treatment procedure is believed to enable a more homogeneous grain size distribution.

In comparison to the LOF sample, the Keyhole sample had a lower volume fraction, and overall size, of intentionally placed discontinuities. A slower scanning speed is known to produce a coarser cellular structure due to the increased time for solute segregation to occur during solidification [88]. In this case, the Keyhole sample also observed an increase in volumetric energy density [89], leading to slower cooling. Slower cooling is understood to have facilitated more recovery to take place, leading to a decrease in GNDs present [14,47,90], as well as enabled more segregated solute to diffuse back in to the γ matrix. The resulting lower density of solute segregation also leads to lower levels of material constraint during subsequent heating and cooling cycles, theoretically leading to a reduced initial build-up of GNDs [51]. Combined, these factors are theorised to have enabled faster grain boundary motion in recrystallised regions as compared to the LOF sample, which was manufactured with higher cooling rates. The volume of plastic deformation and local increase in grain boundary density in this sample was also limited to discrete locations near the position of a keyhole discontinuity, preventing any recrystallisation from occurring at regions surrounding this [47]. Whilst recrystallisation (due to the local increase in plastic deformation by the HIP) was limited to discrete locations in the sample, the increased levels of grain boundary mobility are believed to have enabled discontinuous recrystallisation to occur, leading to the large scale growth of a small number of recrystallised grains alongside non-recrystallised material.

The mechanisms of recrystallisation surrounding these keyhole pores are believed to have remained the same had a larger volume fraction of keyholes been produced in the as-built part. This will however, have facilitated an increased level of compression, triggering the formation of more recrystallisation nuclei within the sample. As an increased number of recrystallisation nuclei leads to an overall finer grain size due to the impingement of growing nuclei on one another, it is understood that as the fraction of keyhole pores increase, the grain size may decrease slightly. However, it is likely that this will still remain larger than the recrystallised grains produced in the LOF sample. This is due to the overall larger as-built grain sizes present in a sample manufactured

using higher energy densities compared to lower energy densities.

The Dense sample was printed with minimal discontinuities and so contained minimal free internal space or surfaces. This led only to a relatively small increase in strain during HIP induced plastic deformation relative to other samples. As a result, despite the large GND density held within the AM grains, large scale recrystallisation was suppressed in this sample as the as-built microstructure did not contain sufficient lattice strain to trigger recrystallisation at the applied temperature without further deformation activities. The dense sample did have fine regions of recrystallised material after HIP. These regions are believed to have been located near fine gas pores that were plastically deformed out of the material during the HIP process. These pores were smaller than keyhole pores and so will have produced a lower density of dislocations during deformation. Indeed, the lack of deformation in the Dense sample, as well as the majority of the Keyhole sample, led to the inability for the AM grain structure to recrystallise at the provided temperature, pressure, and time [47].

Lastly, the Sphere sample was printed with a different internal laser scanning geometry to the other samples. The exact effect of this on the lattice strain in the part cannot be stated without further investigation. In this part, the resulting recrystallised microstructure after HIP is believed to be due to the plastic deformation produced around the powder filled voids. However, as the Sphere Bulk region itself did not include any discontinuities, the bulk deformation in these regions will be less than in the LOF sample, resulting in lower local lattice strains. In addition to the larger grain size attained in this region compared to the LOF sample, this factor led to the formation of a larger overall recrystallised grain size.

Densification of the powder filled (Sphere Void) region is understood to first have occurred through particle sintering due to applied pressure at the elevated temperatures applied during HIP [82,91]. The added effects of high grain boundary area from the powder, HIP induced plastic deformation on the sintered powder (also required in order to break up the external oxide layer on the powder particles), and atomic diffusion at the elevated temperatures, enabled densification and recrystallisation to readily occur. As a result of the gas atomisation process, the powder particles contained a large fraction of fine grain sizes, these being much finer than the grains present in the Sphere Bulk region, leading to final grain diameter of approximately 10 μm. Due to the difference in initial grain size between the AM Sphere Bulk and the encapsulated loose powder, the Sphere sample comprised of two distinct and intentionally placed regions that differed in grain area on average by 97 % after HIP + HT. These regions were separated by a sharp boundary.

Care must be taken when implementing this technique however, with regards to the recyclability and storage of the powder used. Both the LOF and Sphere samples observed Al oxides in their HIP + HT microstructures. This was also reported in similar work on Inconel 718 and blamed for critical weakness in the material [18]. The presence of these oxides reduce the ability for diffusion to occur during densification, making it more difficult to achieve a strong bond between the plastically deformed discontinuity, or powder particle, edges. In addition to this, the Al oxide is brittle, resulting in an easy crack propagation path along the grain boundaries. Oxides were not observed in the samples that underwent complete melting, however the same powder was utilised for the manufacture of all samples in this study. This suggests that the act of melting to a specific temperature allows oxides on the powder surface to escape. The removal of these oxides from the build may occur by spatter, however the mechanisms of this are not currently known. However, this does suggest that when not melted during the AM process, the break-up of oxide regions on powder particles or along the edges of large internal porosities, and the subsequent diffusion of material across the prior boundaries to form a dense microstructure, relies on the plastic deformation applied during the HIP process [92]. Therefore, careful geometric design of the internal void spaces may be required in order to enable the most efficient beak up of oxides during plastic deformation.

Each sample contains an undesirable volume fraction and size of δ-phase particles. This may have occurred due to a number of factors such as the applied strain at elevated temperature, and slow cooling between the homogenisation heat treatment and the double age. In some samples, namely the LOF sample, which underwent recrystallisation during HIP, the δ-phase coarsening is discontinuous at grain boundaries, suggesting supersaturation of the Nb in the matrix [93]. Further to this, is it evident that optimisation of the heat treatment schedule is required for each porosity type separately in order to precipitate an optimised γ″ distribution. This should be investigated with regards to the final part geometry required.

This study also shows that the use of HIP to consolidate fully dense microstructures has the potential to induce inhomogeneous recrystallisation, altering the properties of the material in unintentional locations. As the effects of recrystallisation have been shown to alter the precipitation kinetics of the strengthening phase, this is important to consider when performing HIP on optimised AM parts. This is believed to be exacerbated for complex LPBF geometries and components. Additionally, it should be noted that if HIP is used in order to densify large volumes of discontinuities, or powder encapsulated by an AM structure, the geometric part deformation should be considered in the initial component design stage.

The hardness of each sample in the as-built condition were similar and all lay within measurement variation at approximately ~322–340 Hv. The Dense and Keyhole samples maintained the majority of their strength following HIP due to the retention of cellular substructures inclusive of segregated solute atoms and a high dislocation density, despite their larger grain size. These were eliminated in the Sphere and LOF samples leading to a corresponding drop in hardness that was not compensated from grain refinement. However, the extreme grain refinement in the Sphere Void region rationalises the slight increase in hardness as compared to the other recrystallised samples.

After heat treatment, large variations in the distribution and size of the γ″ precipitates were observed in each sample. Those precipitated in the Keyhole sample are most similar in size and distribution to those observed in the literature, approximately 200 nm in length [94,95]. These were identified within the large discontinuously recrystallised grains in the Keyhole sample. Regions of the Dense sample also exhibited a similar size and distribution of γ″ precipitates. Comparatively, the LOF sample, which underwent large scale recrystallisation, exhibits significantly under-aged γ″ precipitates. Those identified in both regions of the Sphere sample lay between those identified in the LOF, and Keyhole, samples in terms of distribution and size. In comparison to the Dense and Keyhole samples, the additional strengthening provided by the cellular AM sub-structure was also removed in all of the recrystallised samples.

As a consequence, the Dense and Keyhole samples retained a higher level of sub-grain strengthening and a decent level of γ″ strengthening, whilst it is likely that sub-optimal γ″ precipitation was exhibited in the recrystallised samples. This is reflected in the slightly higher hardness values of the non-recrystallised samples after HIP + HT. As previously mentioned, the extreme grain refinement in the Sphere Void region rationalises the slightly higher hardness of this region compared to the other recrystallised samples. The hardness values obtained are similar to those found in other studies [10,84,96,97].

Ultimately, the complex and interdependent strengthening mechanisms in IN718 must be taken into consideration at the design stage, along with additional dynamic mechanical and environmental performance requirements, in order to define the required grain distributions and microstructures for optimised part performance. This extends to variations in component geometry because if constant laser parameters are considered, part geometry largely influences the volume fraction of defects produced. Therefore, a specific use case (component or geometry), should be identified prior to the optimisation of laser parameters for the introduction of a given volume fraction of each discontinuity type. As closed loop control in AM systems becomes more sophisticated, it is envisioned that a desired distribution and pore size can be engineered into a complex part with high levels of accuracy, increasing the

ease at which this method can be implemented.

Overall, these results show that the intentional placement of different characteristic AM discontinuities acts to alter the kinetics of recrystallisation during HIP processing, enabling a range of different final microstructures to be obtained in addition to the typical columnar AM grain morphology. In addition to differences in grain morphology, this technique has shown the potential for large length fractions of $\sum 3$ boundaries to be introduced without the need for additional plastic deformation, as is typically required for grain boundary engineering. Due to their reduced free space and connectivity compared to standard HAGB, the inclusion of these grain boundaries increases the resistance to creep, corrosion, and fatigue based failures, as well as enabling lower electrical resistivity, which are highly desired properties in components designed for advanced engineering applications [46–48,72,98,99].

The HIP process is used as standard for most AM parts intended for high performance applications. In addition to this, further heat treatment is required for all precipitation hardened materials. Therefore, considering the reduction in print time per layer required for the LOF discontinuity region as compared to a dense cylinder interior in this study, 47 %, this method may enable a substantial increase in AM productivity. In addition, this method may enable the production of parts produced from materials which are difficult to fully consolidate using the AM process. Examples of these may be high γ' nickel superalloys which tend to crack during manufacture, or materials with a very fine processing window.

6. Conclusions

The aim of this study was to compare the effects of HIP induced recrystallisation on different types of intentionally placed voids in AM samples in order to understand the potential for these to be used to produce a variety of different functionally graded microstructures. Solution and aging heat treatments were performed to understand the precipitation of strengthening phases in the HIP materials manufactured with different characteristic discontinuities.

It has been demonstrated in this work that the use of different intentionally placed characteristic AM porosities can enable the production of differing grain, and strengthening precipitate, distributions after HIP. Therefore, though the use of a combination of these different porosities within the same part, a variety of different microstructures may be engineered into a single component. This is due to inherent differences in as-built lattice strain concentrations and grain boundary densities produced when printing at the different edges of the material processing window, and is further enabled by differences in the volume and distribution of plastic deformation made possible during the HIP process. It is believed that further optimisation of the spatial distribution of these porosities can enable further control over the microstructure. It is clear that for precipitation hardened materials, each recrystallised microstructure requires a specific post process heat treatment in order to precipitate an optimised volume fraction of strengthening precipitates. It has also been demonstrated that it is possible to retard the recrystallisation process of AM parts if regions of anisotropic mechanical properties are desired.

As the HIP process is used as standard for most AM parts intended for high performance applications, the introduction of a combination of different intentionally placed porosities in the AM part may provide benefits not only to direct component efficiency by enabling functional grading, but also to AM productivity. The potential to manufacture dense parts from difficult to process alloys using AM may also be enhanced if a combination of LOF porosities and HIP post processing can be implemented.

Funding

This work was supported by the UK Engineering and Physical Sciences Research Council [EP/L016273/1], the Manufacture using Advanced Powder Processes (MAPP) EPSRC Future Manufacturing Hub EP/P006566/1, and by Solar Turbines Incorporated. Facilities used at the University of Sheffield, as well access to the TEM at the University of Cambridge, were supported by the Henry Royce Institute through grants EP/R00661X/1, EP/S019367/1, EP/P024947/1 and EP/P025285/1. Access to the TEM was supported by the Henry Royce Institute for advanced materials through the Equipment Access Scheme at Cambridge; Cambridge Royce facilities grant EP/P024947/1 and Sir Henry Royce Institute - recurrent grant EP/R00661X/1.

CRediT authorship contribution statement

E.R. Livera: Writing – review & editing, Writing – original draft, Visualization, Validation, Project administration, Methodology, Investigation, Formal analysis, Data curation, Conceptualization. **K.A. Christofidou:** Writing – review & editing, Supervision, Resources. **J.R. Miller:** Writing – review & editing, Data curation. **L. Chechik:** Writing – review & editing, Conceptualization. **D. Ryan:** Writing – review & editing, Supervision. **J. Shrive:** Data curation. **I. Todd:** Supervision, Resources, Funding acquisition.

Declaration of competing interest

The authors declare that they have no known competing financial interests or personal relationships that could have appeared to influence the work reported in this paper.

Acknowledgements

Thank you to Dr Le Ma (Sorby Centre for Electron Microscopy, University of Sheffield) for collecting the raw EBSD data, Dr Vahid Nekouie (University of Sheffield) for performing the HIP procedure, Neil Hind (University of Sheffield) for performing the heat treatment procedures, Matt Kirkland (University of Sheffield) for performing EDM, and Dr Geoff West (University of Warwick) for preparing the TEM samples.

Supplementary materials

Supplementary material associated with this article can be found, in the online version, at doi:10.1016/j.mtla.2024.102163.

References

[1] E. Paccou, et al., Investigations of powder reusing on microstructure and mechanical properties of Inconel 718 obtained by additive manufacturing, Mater. Sci. Eng. A 828 (June) (2021), https://doi.org/10.1016/j.msea.2021.142113.
[2] T. DebRoy, et al., Additive manufacturing of metallic components – process, structure and properties, Prog. Mater. Sci. 92 (October) (2018) 112–224, https://doi.org/10.1016/j.pmatsci.2017.10.001.
[3] S.A. Khairallah, A.T. Anderson, A. Rubenchik, W.E. King, Laser powder-bed fusion additive manufacturing: physics of complex melt flow and formation mechanisms of pores, spatter, and denudation zones, Acta Mater 108 (2016) 36–45, https://doi.org/10.1016/j.actamat.2016.02.014.
[4] L. Wang, Y. Zhang, H.Y. Chia, W. Yan, Mechanism of keyhole pore formation in metal additive manufacturing, npj Comput. Mater. 8 (1) (2022), https://doi.org/10.1038/s41524-022-00699-6.
[5] W.E. King, et al., Observation of keyhole-mode laser melting in laser powder-bed fusion additive manufacturing, J. Mater. Process. Technol. 214 (12) (2014) 2915–2925, https://doi.org/10.1016/j.jmatprotec.2014.06.005.
[6] W.J. Sames, F.A. List, S. Pannala, R.R. Dehoff, S.S. Babu, The metallurgy and processing science of metal additive manufacturing, Int. Mater. Rev. 61 (5) (2016) 315–360, https://doi.org/10.1080/09506608.2015.1116649.
[7] S.Y. Liu, H.Q. Li, C.X. Qin, R. Zong, X.Y. Fang, The effect of energy density on texture and mechanical anisotropy in selective laser melted Inconel 718, Mater. Des. 191 (2020), https://doi.org/10.1016/j.matdes.2020.108642.
[8] K.N. Amato, et al., Microstructures and mechanical behavior of Inconel 718 fabricated by selective laser melting, Acta Mater 60 (5) (2012) 2229–2239, https://doi.org/10.1016/j.actamat.2011.12.032.
[9] C. Meier, R.W. Penny, Y. Zou, J.S. Gibbs, A.J. Hart, Thermophysical Phenomena in Metal Additive Manufacturing By Selective Laser Melting: fundamentals, Modeling,

Simulation, and Experimentation, Annu. Rev. Heat Transf. 20 (1) (2018) 241–316, https://doi.org/10.1615/annualrevheattransfer.2018019042.
[10] D. Deng, R.L. Peng, H. Brodin, J. Moverare, Microstructure and mechanical properties of Inconel 718 produced by selective laser melting: sample orientation dependence and effects of post heat treatments, Mater. Sci. Eng. A 713 (December) (2018) 294–306, https://doi.org/10.1016/j.msea.2017.12.043.
[11] L. Mugwagwa, D. Dimitrov, S. Matope, I. Yadroitsev, Influence of process parameters on residual stress related distortions in selective laser melting, Procedia Manuf 21 (2018) 92–99, https://doi.org/10.1016/j.promfg.2018.02.099.
[12] K. Moussaoui, W. Rubio, M. Mousseigne, T. Sultan, F. Rezai, Effects of Selective Laser Melting additive manufacturing parameters of Inconel 718 on porosity, microstructure and mechanical properties, Mater. Sci. Eng. A 735 (2018) 182–190, https://doi.org/10.1016/j.msea.2018.08.037.
[13] E. Hosseini, V.A. Popovich, A review of mechanical properties of additively manufactured Inconel 718, Addit. Manuf. 30 (2019), https://doi.org/10.1016/j.addma.2019.100877.
[14] P. Mercelis, J.P. Kruth, Residual stresses in selective laser sintering and selective laser melting, Rapid Prototyp. J. 12 (5) (2006) 254–265, https://doi.org/10.1108/13552540610707013.
[15] T.G. Spears, S.A. Gold, In-process sensing in selective laser melting (SLM) additive manufacturing, Integr. Mater. Manuf. Innov. 5 (2) (2016), https://doi.org/10.1186/s40192-016-0045-4.
[16] V.A. Popovich, E.V. Borisov, A.A. Popovich, V.S. Sufiiarov, D.V. Masaylo, L. Alzina, Functionally graded Inconel 718 processed by additive manufacturing: crystallographic texture, anisotropy of microstructure and mechanical properties, Mater. Des. 114 (2017) 441–449, https://doi.org/10.1016/j.matdes.2016.10.075.
[17] F.S.H.B. Freeman, A. Lincoln, J. Sharp, A. Lambourne, I. Todd, Exploiting thermal strain to achieve an in-situ magnetically graded material, Mater. Des. 161 (2019) 14–21, https://doi.org/10.1016/j.matdes.2018.11.011.
[18] A. Kaletsch, S. Qin, S. Herzog, C. Broeckmann, Influence of high initial porosity introduced by laser powder bed fusion on the fatigue strength of Inconel 718 after post-processing with hot isostatic pressing, Addit. Manuf. 47 (2021), https://doi.org/10.1016/j.addma.2021.102331.
[19] T. Niendorf, S. Leuders, A. Riemer, H.A. Richard, T. Tröster, D. Schwarze, Highly anisotropic steel processed by selective laser melting, Metall. Mater. Trans. B 44B (2013) 794–796, https://doi.org/10.1007/s11663-013-9875-z.
[20] L.N. Carter, C. Martin, P.J. Withers, M.M. Attallah, The influence of the laser scan strategy on grain structure and cracking behaviour in SLM powder-bed fabricated nickel superalloy, J. Alloys Compd. 615 (2014) 338–347, https://doi.org/10.1016/j.jallcom.2014.06.172.
[21] J. Bustillos, J. Kim, A. Moridi, Exploiting lack of fusion defects for microstructural engineering in additive manufacturing, Addit. Manuf. 48 (2021) 102399, https://doi.org/10.1016/j.addma.2021.102399.
[22] R. Esmaeilizadeh, et al., Customizing mechanical properties of additively manufactured Hastelloy X parts by adjusting laser scanning speed, J. Alloys Compd. 812 (2020) 152097, https://doi.org/10.1016/j.jallcom.2019.152097.
[23] S. Gao, R. Liu, R. Huang, X. Song, M. Seita, A hybrid directed energy deposition process to manipulate microstructure and properties of austenitic stainless steel, Mater. Des. 213 (2022) 110360, https://doi.org/10.1016/j.matdes.2021.110360.
[24] V.A. Popovich, E.V. Borisov, V.S. Sufiyarov, A.A. Popovich, Tailoring the properties in functionally graded alloy inconel 718 using additive technologies, Met. Sci. Heat Treat. 60 (11–12) (2019) 701–709, https://doi.org/10.1007/s11041-019-00343-z.
[25] V. Popovich, E. Borisov, T. Riemslag, V. Sufiiarov, Creep and thermomechanical fatigue of functionally graded inconel 718 produced by additive manufacturing, in: TMS 2018 - 147th Annual Meeting and Exhibition, 2018, https://doi.org/10.1007/978-3-319-72526-0.
[26] V.A. Popovich, E.V. Borisov, A.A. Popovich, V.S. Sufiiarov, D.V. Masaylo, L. Alzina, Impact of heat treatment on mechanical behaviour of Inconel 718 processed with tailored microstructure by selective laser melting, Mater. Des. 131 (January) (2017) 12–22, https://doi.org/10.1016/j.matdes.2017.05.065.
[27] B. AlMangour, M.S. Baek, D. Grzesiak, K.A. Lee, Strengthening of stainless steel by titanium carbide addition and grain refinement during selective laser melting, Mater. Sci. Eng. A 712 (October 2017) (2018) 812–818, https://doi.org/10.1016/j.msea.2017.11.126.
[28] D. Jiang, Y. Tian, Y. Zhu, S. Huang, A. Huang, On the microstructure and tensile property of core-shell structured nickel-based superalloy part produced by laser powder bed fusion and hot isostatic pressing, Mater. Sci. Eng. A 870 (February) (2023) 144833, https://doi.org/10.1016/j.msea.2023.144833.
[29] E. Hernández-Nava, P. Mahoney, C.J. Smith, J. Donoghue, I. Todd, S. Tammas-Williams, Additive manufacturing titanium components with isotropic or graded properties by hybrid electron beam melting/hot isostatic pressing powder processing, Sci. Rep. 9 (1) (2019) 1–11, https://doi.org/10.1038/s41598-019-40722-3.
[30] S.H. Sun, T. Ishimoto, K. Hagihara, Y. Tsutsumi, T. Hanawa, T. Nakano, Excellent mechanical and corrosion properties of austenitic stainless steel with a unique crystallographic lamellar microstructure via selective laser melting, Scr. Mater. 159 (2019) 89–93, https://doi.org/10.1016/j.scriptamat.2018.09.017.
[31] F.S.H.B. Freeman, L.M. Jones, A.D. Goodall, H. Ghadbeigi, I. Todd, Structural metamaterial lattices by laser powder-bed fusion of 17-4PH steel, Addit. Manuf. Lett. 8 (December 2023) (2024) 100190, https://doi.org/10.1016/j.addlet.2023.100190.
[32] K.A. Sofinowski, S. Raman, X. Wang, B. Gaskey, M. Seita, Layer-wise engineering of grain orientation (LEGO) in laser powder bed fusion of stainless steel 316L, Addit. Manuf. 38 (2021) 101809, https://doi.org/10.1016/j.addma.2020.101809.
[33] S. Ghorbanpour, et al., Effect of microstructure induced anisotropy on fatigue behaviour of functionally graded Inconel 718 fabricated by additive manufacturing, Mater. Charact. 179 (May) (2021) 111350, https://doi.org/10.1016/j.matchar.2021.111350.
[34] D.D.R. Peachey, et al., Directional recrystallization of an additively manufactured Ni-base superalloy, Addit. Manuf. 60 (PA) (2022) 103198, https://doi.org/10.1016/j.addma.2022.103198.
[35] H.E. Sabzi, et al., Grain refinement in laser powder bed fusion: the influence of dynamic recrystallization and recovery, Mater. Des. 196 (2020), https://doi.org/10.1016/j.matdes.2020.109181.
[36] S. Tammas-Williams, P.J. Withers, I. Todd, P.B. Prangnell, Porosity regrowth during heat treatment of hot isostatically pressed additively manufactured titanium components, Scr. Mater. 122 (2016) 72–76, https://doi.org/10.1016/j.scriptamat.2016.05.002.
[37] H.V. Atkinson, S. Davies, Fundamental aspects of hot isostatic pressing : an overview, Metall. Mater. Trans. A 31 (December) (2000) 2981–3000, https://doi.org/10.1007/s11661-000-0078-2.
[38] A. du Plessis, E. Macdonald, Hot isostatic pressing in metal additive manufacturing: x-ray tomography reveals details of pore closure, Addit. Manuf. 34 (February) (2020) 101191, https://doi.org/10.1016/j.addma.2020.101191.
[39] W. Tillmann, C. Schaak, J. Nellesen, M. Schaper, M.E. Aydinöz, K.P. Hoyer, Hot isostatic pressing of IN718 components manufactured by selective laser melting, Addit. Manuf. 13 (November) (2017) 93–102, https://doi.org/10.1016/j.addma.2016.11.006.
[40] W. Tillmann, et al., Functional encapsulation of laser melted Inconel 718 by Arc-PVD and HVOF for post compacting by hot isostatic pressing Functional encapsulation of laser melted Inconel 718 by Arc-PVD and HVOF for post compacting by hot isostatic pressing, Powder Metall 58 (4) (2015) 259–264, https://doi.org/10.1179/0032589915Z.000000000250.
[41] A. du Plessis, P. Rossouw, Investigation of porosity changes in Cast Ti6Al4V rods after hot isostatic pressing, J. Mater. Eng. Perform. 24 (8) (2015) 3137–3141, https://doi.org/10.1007/s11665-015-1580-4.
[42] S. Tammas-williams, P.J. Withers, I. Todd, P.B. Prangnell, The effectiveness of hot isostatic pressing for closing porosity in selective electron beam melting, Metall. Mater. Trans. A 47A (5) (2016) 1939–1946, https://doi.org/10.1007/s11661-016-3429-3.
[43] S.Y. Park, K.S. Kim, M.C. Kim, M.E. Kassner, K.A. Lee, Effect of Post-heat treatment on the tensile and cryogenic impact toughness properties of inconel 718 manufactured by selective laser melting, Adv. Eng. Mater. 23 (3) (2021), https://doi.org/10.1002/adem.202001005.
[44] Y.J. Kang, S. Yang, Y.K. Kim, B. AlMangour, K.A. Lee, Effect of post-treatment on the microstructure and high-temperature oxidation behaviour of additively manufactured inconel 718 alloy, Corros. Sci. 158 (June) (2019) 108082, https://doi.org/10.1016/j.corsci.2019.06.030.
[45] M.E. Aydinöz, et al., On the microstructural and mechanical properties of post-treated additively manufactured Inconel 718 superalloy under quasi-static and cyclic loading, Mater. Sci. Eng. A 669 (May) (2016) 246–258, https://doi.org/10.1016/j.msea.2016.05.089.
[46] F.J. Humphreys, M. Hatherly, Recrystallization and Related Annealing Phenomena, 2nd ed., Elsevier Ltd, 2004.
[47] S. Gao, et al., Recrystallization-based grain boundary engineering of 316L stainless steel produced via selective laser melting, Acta Mater 200 (2020) 366–377, https://doi.org/10.1016/j.actamat.2020.09.015.
[48] B. Liu, et al., Grain boundary engineering activated by residual stress during the laser powder bed fusion of Inconel 718 and the electrochemical corrosion performance, Mater. Charact. 204 (July) (2023), https://doi.org/10.1016/j.matchar.2023.113160.
[49] R.W. Cahn, Recovery and Recrystallization. Physical Metallurgy, North-Holland Printing Company, 1965, pp. 925–985.
[50] L.R. Owen, N.G. Jones, Lattice distortions in high-entropy alloys, J. Mater. Res. 33 (19) (2018) 2954–2969, https://doi.org/10.1557/jmr.2018.322.
[51] S. Tekumalla, M. Seita, S. Zaefferer, Delineating dislocation structures and residual stresses in additively manufactured alloys, Acta Mater 262 (October 2023) (2024) 119413, https://doi.org/10.1016/j.actamat.2023.119413.
[52] D. Kong, et al., About metastable cellular structure in additively manufactured austenitic stainless steels, Addit. Manuf. 38 (September 2020) (2021) 101804, https://doi.org/10.1016/j.addma.2020.101804.
[53] K.M. Bertsch, G. Meric de Bellefon, B. Kuehl, D.J. Thoma, Origin of dislocation structures in an additively manufactured austenitic stainless steel 316L, Acta Mater 199 (2020) 19–33, https://doi.org/10.1016/j.actamat.2020.07.063.
[54] M. Godec, S. Zaefferer, B. Podgornik, M. Šinko, E. Tchernychova, Quantitative multiscale correlative microstructure analysis of additive manufacturing of stainless steel 316L processed by selective laser melting, Mater. Charact. 160 (December 2019) (2020), https://doi.org/10.1016/j.matchar.2019.110074.
[55] M. Zouari, R.E. Logé, N. Bozzolo, In situ characterization of inconel 718 post-dynamic recrystallization within a scanning electron microscope, Metals (Basel) 7 (266) (2017), https://doi.org/10.3390/met7110476.
[56] R.W.K. Honeycombe, The Plastic Deformation of Metals, Edward Arnold (Publishers) Ltd., 1968.
[57] Y.C. Lin, et al., EBSD study of a hot deformed nickel-based superalloy, J. Alloys Compd. 640 (2015) 101–113, https://doi.org/10.1016/j.jallcom.2015.04.008.
[58] F. Brenne, et al., Microstructural design of Ni-base alloys for high-temperature applications: impact of heat treatment on microstructure and mechanical properties after selective laser melting, Prog. Addit. Manuf. 1 (3–4) (2016) 141–151, https://doi.org/10.1007/s40964-016-0013-8.
[59] S. Raghavan, et al., Effect of different heat treatments on the microstructure and mechanical properties in selective laser melted INCONEL 718 alloy, Mater. Manuf.

Process. 32 (14) (2017) 1588–1595, https://doi.org/10.1080/10426914.2016.1257805.
[60] J. Schneider, B. Lund, M. Fullen, Effect of heat treatment variations on the mechanical properties of Inconel 718 selective laser melted specimens, Addit. Manuf. 21 (December 2017) (2018) 248–254, https://doi.org/10.1016/j.addma.2018.03.005.
[61] W.M. Tucho, V. Hansen, Studies of post-fabrication heat treatment of L-PBF-inconel 718: effects of hold time on microstructure, annealing twins, and hardness, Metals (Basel) 11 (2) (2021) 1–20, https://doi.org/10.3390/met11020266.
[62] D.A. Porter, K.E. Easterling, M.Y. Sherif, Crystal interfaces and microstructure. Phase Transformations in Metals and Alloys, Chapman & Hall, 2009.
[63] I. Radomir, V. Geamăn, M. Stoicănescu, Densification mechanisms made during creep techniques applied to the hot isostatic pressing, Procedia - Soc. Behav. Sci. 62 (2012) 779–782, https://doi.org/10.1016/j.sbspro.2012.09.131.
[64] M. Azarbarmas, M. Aghaie-Khafri, J.M. Cabrera, J. Calvo, Dynamic recrystallization mechanisms and twining evolution during hot deformation of Inconel 718, Mater. Sci. Eng. A 678 (September) (2016) 137–152, https://doi.org/10.1016/j.msea.2016.09.100.
[65] D. Raabe, "Recovery and Recrystallization: phenomena, Physics, Models, Simulation," in *Physical Metallurgy*, 5th Edit., vol. 1, D. E. Laughlin and K. Hono, Eds. Elsevier, 2014, pp. 2291–2397. https://doi.org/10.1016/B978-0-444-53770-6.00023-X.
[66] T. Sakai, A. Belyakov, R. Kaibyshev, H. Miura, J.J. Jonas, Dynamic and post-dynamic recrystallization under hot, cold and severe plastic deformation conditions, Prog. Mater. Sci. 60 (1) (2014) 130–207, https://doi.org/10.1016/j.pmatsci.2013.09.002.
[67] H. Beladi, P. Cizek, P.D. Hodgson, Dynamic recrystallization of austenite in Ni-30 Pct Fe model alloy: microstructure and texture evolution, Metall. Mater. Trans. A Phys. Metall. Mater. Sci. 40 (5) (2009) 1175–1189, https://doi.org/10.1007/s11661-009-9799-z.
[68] Y. In, B. Lin, A.D. Rollett, G.S. Rohrer, M. Bernacki, N. Bozzolo, Thermo-mechanical factors influencing annealing twin development in nickel during recrystallization, J. Mater. Sci. 50 (15) (2015) 5191–5203, https://doi.org/10.1007/s10853-015-9067-0.
[69] A.M. Wusatowska-Sarnek, H. Miura, T. Sakai, Nucleation and microtexture development under dynamic recrystallization of copper, Mater. Sci. Eng. A 323 (1–2) (2002) 177–186, https://doi.org/10.1016/S0921-5093(01)01336-3.
[70] H. Zhang, K. Zhang, H. Zhou, Z. Lu, C. Zhao, X. Yang, Effect of strain rate on microstructure evolution of a nickel-based superalloy during hot deformation, Mater. Des. 80 (2015) 51–62, https://doi.org/10.1016/j.matdes.2015.05.004.
[71] S. Holland, X. Wang, X.Y. Fang, Y.B. Guo, F. Yan, L. Li, Grain boundary network evolution in Inconel 718 from selective laser melting to heat treatment, Mater. Sci. Eng. A 725 (April) (2018) 406–418, https://doi.org/10.1016/j.msea.2018.04.045.
[72] W. Wang, et al., Influence of stored energy on twin formation during primary recrystallization, Mater. Sci. Eng. A 589 (2014) 112–118, https://doi.org/10.1016/j.msea.2013.09.071.
[73] U.S. Bertoli, A.J. Wolfer, M.J. Matthews, J.P.R. Delplanque, J.M. Schoenung, On the limitations of Volumetric Energy Density as a design parameter for Selective Laser Melting, Mater. Des. 113 (2017) 331–340, https://doi.org/10.1016/j.matdes.2016.10.037.
[74] J. Schindelin, et al., Fiji : an open-source platform for biological-image analysis, Nat. Methods 9 (7) (2012), https://doi.org/10.1038/nmeth.2019.
[75] F. Bachmann, R. Hielscher, H. Schaeben, Grain detection from 2d and 3d EBSD data-Specification of the MTEX algorithm, Ultramicroscopy 111 (12) (2011) 1720–1733, https://doi.org/10.1016/j.ultramic.2011.08.002.
[76] M.N. Ahsan, R. Bradley, A.J. Pinkerton, Microcomputed tomography analysis of intralayer porosity generation in laser direct metal deposition and its causes, J. Laser Appl. 23 (2) (2011) 022009, https://doi.org/10.2351/1.3582311.
[77] G. Kasperovich, J. Haubrich, J. Gussone, G. Requena, Correlation between porosity and processing parameters in TiAl6V4 produced by selective laser melting, Mater. Des. 105 (2016) 160–170, https://doi.org/10.1016/j.matdes.2016.09.040.
[78] S. Azadian, L.Y. Wei, R. Warren, Delta phase precipitation in inconel 718, Mater. Charact. 53 (1) (2004) 7–16, https://doi.org/10.1016/j.matchar.2004.07.004.
[79] N.C. Ferreri, S.C. Vogel, M. Knezevic, Determining volume fractions of γ, γ′, γ″, δ, and MC-carbide phases in Inconel 718 as a function of its processing history using an advanced neutron diffraction procedure, Mater. Sci. Eng. A 781 (January) (2020) 139228, https://doi.org/10.1016/j.msea.2020.139228.
[80] G.H. Cao, et al., Investigations of γ′ γ″ and δ precipitates in heat-treated Inconel 718 alloy fabricated by selective laser melting, Mater. Charact. 136 (January) (2018) 398–406, https://doi.org/10.1016/j.matchar.2018.01.006.
[81] W.M. Tucho, V. Hansen, Characterization of SLM-fabricated Inconel 718 after solid solution and precipitation hardening heat treatments, J. Mater. Sci. 54 (1) (2019) 823–839, https://doi.org/10.1007/s10853-018-2851-x.
[82] H. Yu, X. Liu, X. Li, A. Godbole, Crack healing in a low-carbon steel under hot plastic deformation, Metall. Mater. Trans. A Phys. Metall. Mater. Sci. 45 (2) (2014) 1001–1009, https://doi.org/10.1007/s11661-013-2049-4.
[83] F. Liu, X. Lin, G. Yang, M. Song, J. Chen, W. Huang, Microstructure and residual stress of laser rapid formed Inconel 718 nickel-base superalloy, Opt. Laser Technol. 43 (1) (2011) 208–213, https://doi.org/10.1016/j.optlastec.2010.06.015.
[84] W.M. Tucho, V. Hansen, Studies of Post-Fabrication Heat Treatment of L-PBF-Inconel 718: effects of Hold Time on Microstructure, Annealing Twins, and Hardness, Metals (Basel) 11 (266) (2021), https://doi.org/10.3390/met11020266.
[85] Y.C. Lin, et al., EBSD analysis of evolution of dynamic recrystallization grains and δ phase in a nickel-based superalloy during hot compressive deformation, Mater. Des. 97 (2016) 13–24, https://doi.org/10.1016/j.matdes.2016.02.052.
[86] P.C. Yadav, S. Sahu, A. Subramaniam, S. Shekhar, Effect of heat-treatment on microstructural evolution and mechanical behaviour of severely deformed Inconel 718, Mater. Sci. Eng. A 715 (January) (2018) 295–306, https://doi.org/10.1016/j.msea.2018.01.007.
[87] W. Yinmin, C. Mingwei, Z. Fenghua, M. En, High tensile ductility in a nanostructured metal, Nature 419 (6910) (2002) 912–914, https://doi.org/10.1038/nature01133 [Online]. Available:.
[88] W. Kurz, D.J. Fisher, Fundamentals of Solidification, 4th ed., Trans Tech Publications Ltd, 1998.
[89] M. Thomas, G.J. Baxter, I. Todd, Normalised model-based processing diagrams for additive layer manufacture of engineering alloys, Acta Mater 108 (2016) 26–35, https://doi.org/10.1016/j.actamat.2016.02.025.
[90] L. Parry, I.A. Ashcroft, R.D. Wildman, Understanding the effect of laser scan strategy on residual stress in selective laser melting through thermo-mechanical simulation, Addit. Manuf. 12 (2016) 1–15, https://doi.org/10.1016/j.addma.2016.05.014.
[91] W. Duan, Y. Yin, J. Zhou, M. Wang, H. Nan, P. Zhang, Dynamic research on Ti6Al4V powder HIP densification process based on intermittent experiments, J. Alloys Compd. 771 (2019) 489–497, https://doi.org/10.1016/j.jallcom.2018.08.261.
[92] Y. Wang, Y. Liu, S.D. Pay, B. Lan, J. Jiang, A study of solid-state bonding-by-hot-deforming mechanism in Inconel 718, J. Mater. Process. Technol. 295 (January) (2021) 117191, https://doi.org/10.1016/j.jmatprotec.2021.117191.
[93] I. Manna, S.K. Pabi, W. Gust, Discontinuous reactions in solids, Int. Mater. Rev. 46 (2) (2001) 53–91, https://doi.org/10.1179/095066001101528402.
[94] A. Devaux, et al., Gamma double prime precipitation kinetic in Alloy 718, Mater. Sci. Eng. A 486 (1–2) (2008) 117–122, https://doi.org/10.1016/j.msea.2007.08.046.
[95] P.M. Mignanelli, et al., Gamma-gamma prime-gamma double prime dual-superlattice superalloys, Scr. Mater. 136 (2017) 136–140, https://doi.org/10.1016/j.scriptamat.2017.04.029.
[96] J. Strößner, M. Terock, U. Glatzel, Mechanical and microstructural investigation of nickel-based superalloy IN718 manufactured by selective laser melting (SLM), Adv. Eng. Mater. 17 (8) (2015) 1099–1105, https://doi.org/10.1002/adem.201500158.
[97] S. Periane, et al., Influence of heat treatment on the fatigue resistance of inconel 718 fabricated by selective laser melting (SLM), Mater. Today Proc. 46 (March) (2021) 7860–7865, https://doi.org/10.1016/j.matpr.2021.02.447.
[98] V. Randle, Twinning-related grain boundary engineering, Acta Mater 52 (14) (2004) 4067–4081, https://doi.org/10.1016/j.actamat.2004.05.031.
[99] V. Randle, Mechanism of twinning-induced grain boundary engineering in low stacking-fault energy materials, Acta Metall. Inc 47 (15) (1999) 4187–4196, https://doi.org/10.1016/S1359-6454(99)00277-3.